18TH WORLD CONFERENCE ON EARTHQUAKE ENGINEERING
WCEE2024
MILAN

MILAN, ITALY
30TH JUNE - 5TH JULY 2024

www.wcee2024.it

SEISMIC RESPONSE OF UNBONDED PRECAST POST-TENSIONED BRIDGE PIERS WITH MULTI-ROCKING INTERFACES

Y. Shen[1], F. Freddi [2] & J. Li[3]

[1] Department of Bridge Engineering, Tongji University, Shanghai, China, yushen@tongji.edu.cn

[2] Department of Civil, Environmental & Geomatic Engineering, University College London, London, UK

[3] State Key Laboratory of Disaster Reduction in Civil Engineering, Tongji University, Shanghai, China

Abstract: *In the last few decades, several research studies have focused on the development of unbonded post-tensioned (PT) bridge piers defined according to accelerated bridge construction (ABC) techniques. These solutions showed several advantages in terms of minimal damage seismic response, hence promoting the objectives of seismic resilient structures of modern societies. These piers can be built with either a single rocking interface at the base or multiple rocking interfaces along the pier height. The present paper investigates and compares the design and seismic response of unbonded PT bridge piers with base or multi-rocking interfaces. Bridge piers previously tested by the authors and showing single or multiple rocking interfaces are considered for case study purposes. Finite element models are developed in OpenSees, including mechanical and geometric non-linearities, and validated against the experimental results. Non-linear time-history analyses are performed in an Incremental Dynamic Analyses (IDAs) fashion to evaluate the seismic response of each configuration. IDAs are carried out with two sets of pulse-like and no-pulse-like ground motions, respectively. The results highlight the differences in the seismic response of the two types of bridge piers and the two sets of records. Compared to the base rocking bridge piers, multi-rocking pier systems show a larger rocking-related response (e.g., the lateral displacement), while their acceleration-related response (e.g., the shear force) was comparable. On the other side, the multi-rocking pier mechanism results in a more severe PT force loss. In addition, the pulse-like feature of the ground motions can, to some extent, amplify the seismic responses related to the pier's deformation. The paper provides useful insights into the optimal design of seismic resilient unbonded PT bridge piers.*

1 Introduction

In recent years, stakeholders have made significant efforts to promote the use of accelerated bridge construction (ABC) techniques. Such technologies can reduce construction-related disruptions to traffic infrastructure and, if properly designed, enhance resilience under extreme natural events, *e.g.,* earthquakes, floods, and tsunamis (NCHRP 2011). At the same time, several research studies demonstrated the considerable direct and indirect losses deriving from high-intensity earthquake events, representing one of the deadliest and costliest forms of disaster (Freddi *et al.* 2021). In this context, the use of innovative ABC techniques represents an opportunity to reduce such losses and improve seismic resilience. However, several aspects related to the design and implementation of such technologies need to be addressed, especially for highly seismic-prone areas.

Unbonded post-tensioned reinforced concrete (PRC) bridge piers serve as a seismic-resilient ABC alternative to the traditional cast-in-place piers due to their excellent seismic performance in terms of low damage, re-centering capacity, and high ductility (*e.g.,* Marriott et al 2009; Mashal and Palermo 2019; Shen *et al.* 2022, 2023a, 2023b). PRC piers use post-tensioned (PT) bars/tendons to connect the precast pier column or multiple precast pier segments to the foundations to provide the self-centering behavior (*i.e.,* corresponding to the single base rocking interface or the multiple rocking interface mechanisms) and adopt energy-dissipating (ED) devices/bars at specific interfaces to dissipate the seismic input energy. Figures 1(a) and 1(b), respectively, show a schematic deformation response of the PRC pier designed with a single base interface and multiple interfaces under earthquake excitation. As the precast pier column displaces laterally along the excitation direction, the evident gap opening is formed at the interfaces between the pier base and the foundation or between the adjacent segments as the column/segments rotate rigidly about their compression toes (*i.e.,* the rocking behavior). Under this situation, both the PT and ED bars are stretched accordingly, providing the pier's self-centering and ED capacities. The response is characterized by a typical flag-shaped cycle response with small residual displacement (Elettore *et al.* 2022), as shown in Figure 1(c).

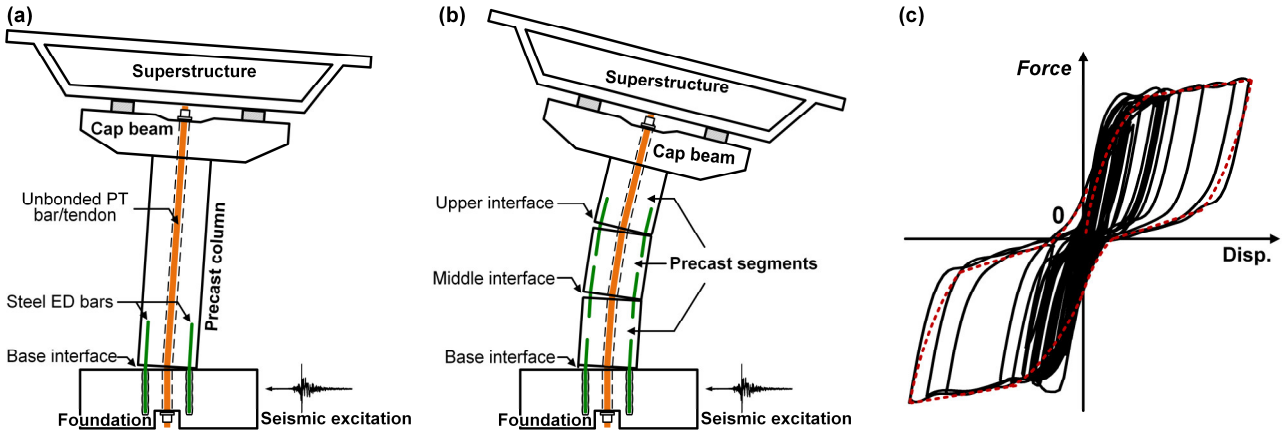

Figure 1. Typical PRC piers: (a) idealized deformation mode with a single base rocking interface; (b) idealized deformation mode with multiple rocking interfaces; and (c) flag-shaped hysteretic response.

The seismic performance of PRC bridge piers has been experimentally and numerically investigated by many researchers. Among others, Marriott *et al.* (2009) compared the cyclic behavior, construction techniques, and damage states between precast PRC piers and monolithic cast-in-place reinforced concrete (RC) piers through both quasi-static and pseudo-dynamic tests, indicating the significant promise for the application of PRC piers in seismic regions. Kwan and Billington (2003a, 2003b) performed numerical studies to comprehensively investigate PRC piers' monotonic, cyclic, and seismic responses, showing their superior performance in terms of reduced residual deformations. Shen *et al.* (2022) presented a parametric experimental campaign on PRC piers with various initial PT forces, ED bar ratios, and unbonded lengths of ED bars to identify the effects of these parameters on the cyclic response. Additional studies investigated several solutions to minimize further the concrete damage caused by the local compression stress around the rocking toe. Several solutions were proposed, including the use of confinement by a tube/jacket (Hassanli *et al.* 2017; Shen *et al.* 2023a), the casting of novel cementitious materials (Billington and Yoon 2004; Trono *et al.* 2015; Shen *et al.* 2023a), and the arming with the mechanical hinges (Freddi *et al.* 2020; Zhong *et al.* 2022), among others. In addition, Yamashita and Sanders (2009), Trono *et al.* (2015), and Shen *et al.* (2023b) carried out shake table tests of various versions of PRC piers and found similar results.

Although the abovementioned literature confirmed the merits and advantages provided by rocking mechanisms in bridge piers, the studies focusing on the effects of the rocking interface number on the seismic behavior are limited, in particular under some particular earthquake scenarios (*e.g.,* pulse-like records) due to their complex non-linear behavior. To this end, this paper numerically investigates the seismic response of three PRC piers with an increasing number of rocking interfaces (*i.e.,* one, two, and three). One is designed to rock only at the pier base, and the others have, respectively, two and three rocking interfaces along the pier height (*i.e.,* multi-rocking interfaces). Finite element (FE) models for these three PRC piers have been developed and validated against the available experimental results. The comparison of the seismic responses

of the three PRC piers considering different records and different intensities is then carried out by Incremental Dynamic Analyses (IDAs). Two sets of records considering far-field and near-fault ground motions have been considered to investigate the influence of the velocity pulse.

2 Description of test specimens and campaign

The present study takes advantage of the experimental results of two PRC specimens (identified as Specimens PRC and PRC+ST) previously tested by the Authors (Shen *et al.* 2023b) to validate the FE models. Both specimens were designed and constructed to meet the requirements of the shake table, and Figure 2 shows the two specimens and their experimental setup. Each pier column of specimens had a circular section with a diameter of 440 mm. A rigid footing and a concrete mass block with dimensions of 1.76 × 1.26 × 0.60 m and 2.50 × 2.50 × 0.55 m, respectively, were located at the bottom and top of the column. The clear height of the column, from its base to the bottom of the concrete mass block, was 1.35 m. Four diagonal steel braces were used at the top of the pier column to provide a rigid connection between the column and the mass block. Six mild bars with a diameter of 16 mm were used as ED bars, corresponding to a reinforcing ratio of 0.79%. A sufficient unbonded length of 25 cm was provided in the ED bars to avoid premature fracture during rocking. The PT bar was a 40 mm diameter high-strength threaded steel bar, with an initial post-tensioning force of 749 kN. In Specimen PRC, the pier column was designed without enhanced details [Figure 2(a)], while the Specimen PRC+ST used a steel tube with an outer diameter of 440 mm and a thickness of 6 mm as a jacket for the pier base to mitigate the concrete damage [Figure 2(b)]. It should be noted that, in order to produce an identical axial compressive ratio of 7.5% as in the prototype bridge pier, twelve iron blocks were added to the top of the concrete block after the specimen was placed on the shake table, as shown in Figure 2(c).

Figure 2. Views of test specimens: (a) PRC; (b) PRC+ST; and (c) their test setup [from Shen et al. 2003b].

The loading protocol of the shake table test is divided into three phases: elastic response level test, design basis earthquake (DBE) level test, and large intensity level test. In this study, only the test results at the DBE level were used for the FE model validation, as the pier damage was minor, and the obvious rocking response was induced at this test level. Three earthquake recorders with a peak ground acceleration (PGA) of 0.3g were used as input motions for this test level, as shown in Figure 3. They are the 1940 El Centro ground motion, the 1971 San Fernando ground motion, and the 1999 Chi-Chi ground motion. Note that the original time axis of three ground motions was reduced by a factor of 0.459 before testing to account for the scaling of the specimen (Lu *et al.* 2008).

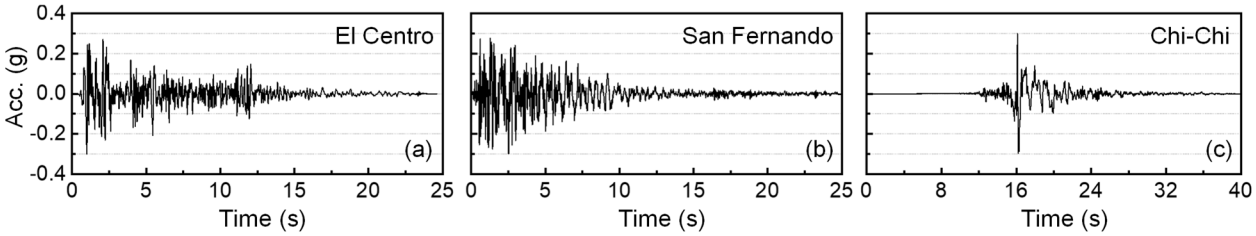

Figure 3. Input ground motions at the Design Based Earthquake (DBE) level.

The Specimen PRC exhibited a base rocking behavior during the DBE level tests. In contrast, the Specimen PRC+ST experienced multi-rocking mechanisms with rocking interfaces at the base and the enhanced ST segment upper interface.

3 Finite element (FE) modeling and validation

Three-dimensional FE models of PRC piers with different rocking interfaces were developed in OpenSees (Mazzoni *et al.* 2009). The FE modeling strategy, the assumptions (*e.g.,* material properties, contact models, and PT force loss), and the validation are described in the following sections. It is worth mentioning that the validation of the multi-rocking interface modeling (Section 3.2) was carried out only for the PRC with two rocking interfaces due to the available test results.

3.1 Single rocking interface modeling

Figure 4 shows the PRC numerical model with the single rocking interface at the pier base. A lumped mass was placed at the location of the mass center in the experimental test to represent the mass of the superstructure (*i.e.,* the mass blocks). Conversely, the mass of the column was distributed by five mass nodes along the pier height [Figure 4(a)]. The center of mass was connected with the pier top using the rigid link element, while the pier column was simulated by the displacement-based non-linear beam-column element in OpenSees. The uniaxial material models of 'Concrete01' and 'Steel02' in OpenSees were used for the column concrete and the longitudinal steel, respectively. The PT bar was modeled by an elastic truss element and connected the footing at the bottom and the mass block at the top. Initial post-tensioning force F_{PT0} in the PT bar was applied by the 'Initial Strain Material' (Elettore *et al.* 2021). The mechanical behavior of ED bars was described using the 'Hysteretic' material model in OpenSees with three turning points, as shown in Figure 4(b). These three points corresponded to the yielding (ε_{y_ED}, f_{y_ED}), peak (ε_{p_ED}, f_{p_ED}), and ultimate (ε_{u_ED}, f_{u_ED}) states of the ED bars and were determined based on material tensile tests. Note that the length of the ED bar elements should consider the strain penetration at both ends (Bu *et al.* 2016). The top of the ED bar elements was rigidly connected to the intermediate node of the pier column.

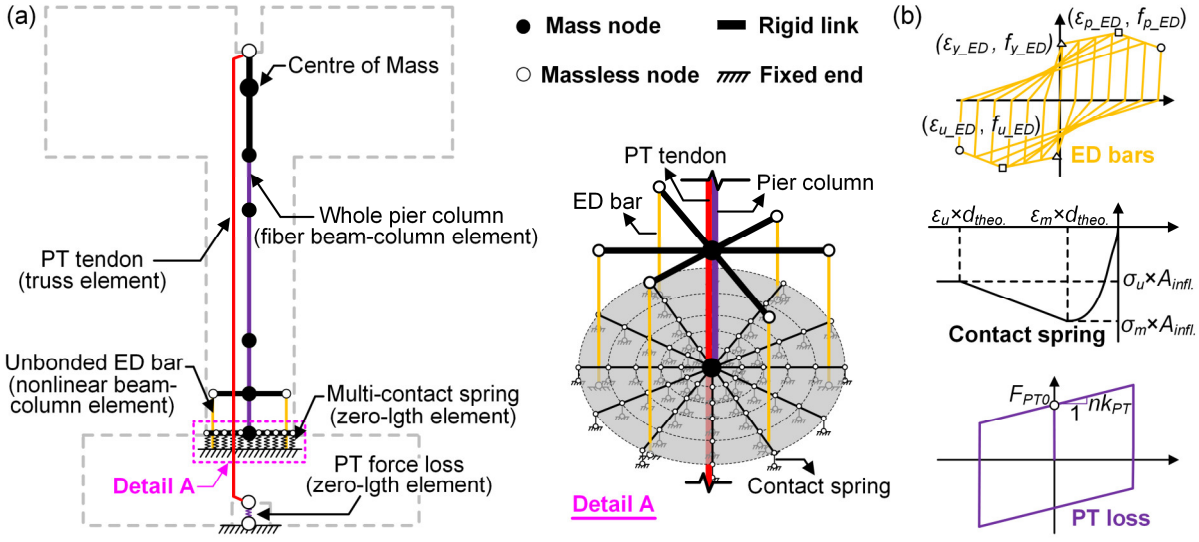

Figure 4. Finite Element (FE) model of single-rocking interface pier: (a) model sketches; (b) model details.

To model contacts, a series of zero-length spring elements with compression-only properties were used [Detail A in Figure 4(a)]. The compression-only behavior was obtained by using the compression-only 'Concrete01' material [Figure 4(b)]. Being the contact springs discrete within the interface, the compressive behavior of each contact element was defined by assigning a force-displacement relationship following the recommendations of Guerrini *et al.* (2015) and Li *et al.* (2021), *i.e.,* the stress (σ) and strain (ε) of the interface material were amplified by the spring influence area (A_{infl}) and theoretical neutral axial depth (d_{theo}), respectively. In this study, the d_{theo} was set as 1/4 times the column diameter. A PT force loss was observed during the tests due to the inelastic behavior of several components, such as the plastic damage of the pier column and the anchorage seating losses. This PT force loss was considered in the FE model by introducing a zero-length element with

multilinear material between the bottom end of the PT element and the fixed boundary [Figure 4(a)]. The stiffness of this zero-length element was set equal to n times the axial stiffness of PT bar (k_{PT}), *i.e.,* nk_{PT}, as shown in Figure 4(b), where the parameter n was related to the amount of PT loss, the elongation of PT bar and the type of PRC piers. Detailed information about the calibration of the model for the PT force loss can be found in Shen *et al.* (2022; 2023a). In addition, only Rayleigh damping with a damping ratio value of 5% was used in the FE simulations to consider the damping properties, while the damping effect provided by the contacts at the rocking interface was neglected.

3.2 Multiple rocking interface modeling

Figure 5 shows the FE model of the PRC pier with two/three-rocking interfaces, *i.e.,* the multiple rocking interface models. The element types and material properties of the multiple rocking interface model were identical to those used in the single rocking interface model. The only difference was the number of rocking interfaces and the contact properties [Figure 5(a)]. As previously mentioned, the properties of the contact springs were related to the interface material, and thus, the stress-strain (or force-displacement) relationship of the contact elements should be adjusted according to the corresponding pier segment materials. In addition, additional nodes and elements were included to simulate the different segments of the pier column and the multiple rocking interfaces [Details B and C in Figures 5(b) and 5(c)].

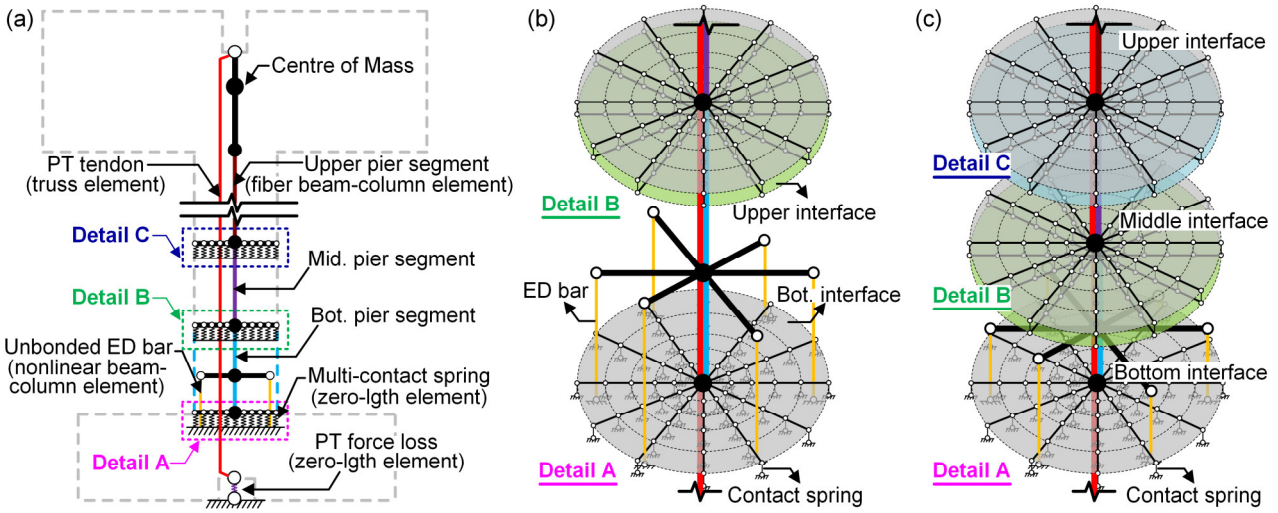

Figure 5. Finite Element (FE) model of the multiple-rocking interface pier: (a) model sketches; (b) two-rocking interface details; and (c) three-rocking interface details.

3.3 Validation of the Finite Element (FE) models

The Specimens PRC was selected as the validation case of the single rocking response. Figure 6 shows the comparison of its seismic responses obtained from the FE analyses (the red dotted line) and tests (the black solid line) under three ground motions. Figure 6(a) shows that the displacement responses at the mass center predicted by the FE model were in good agreement with the test results. In particular, the peak displacements of the El Centro, San Fernando, and Chi-Chi ground motions obtained by the FE simulations were 0.28, 0.39, and 0.34 m, respectively, while the corresponding test results were almost identical with values of 0.27, 0.41, and 0.33 m, respectively. The acceleration results of the PRC pier with the single rocking interface estimated by the FE model and the experimental test also agreed well, as shown in Figure 6(b).

Similarly, Figure 7 shows the comparison of the seismic responses obtained from the FE analyses and tests for the Specimen PRC+ST (*i.e.,* the case of two rocking interfaces). Figure 7 shows that the simulation results of all three ground motions demonstrated a good agreement with the test results in terms of lateral displacements, shear forces, and PT forces. For example, the errors in the maximum PT force between the numerical analysis and the shake table test were only 2.3%, 0.9%, and 1.7% for the El Centro, San Fernando, and Chi-Chi ground motions, respectively. The PT force loss was also reproduced by the FE model, as shown in Figure 7(c). A PT loss of 8.2, 2.3, and 3.8 kN was recorded in the tests for the El Centro, San Fernando, and Chi-Chi ground motions, respectively. The corresponding FE simulation results were 10.1, 2.9, and 2.5 kN, respectively. The experimental results were in good agreement with the numerical results, which shows

that the developed FE model with multiple rocking interfaces was able to predict the seismic response of two rocking interfaces. Although a validation was not conducted for PRC piers with more rocking interfaces (*e.g.,* three rocking interfaces), it is expected that the model is equally able to capture the seismic response of the system with reasonable confidence.

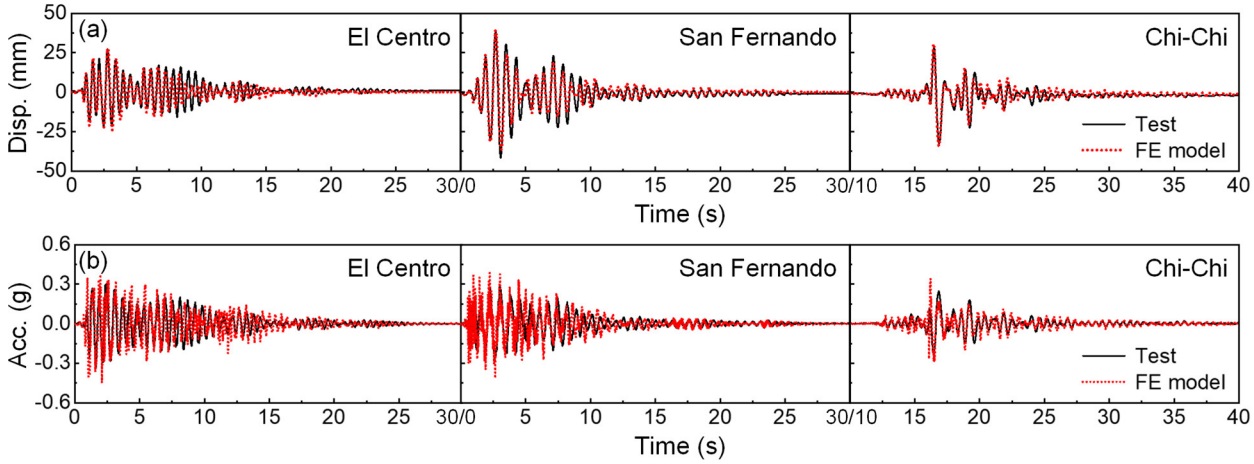

Figure 6. Comparisons between FE and test results of the single-rocking interface pier (i.e., the PRC specimen): (a) displacement histories at the mass center; (b) acceleration histories at the mass center.

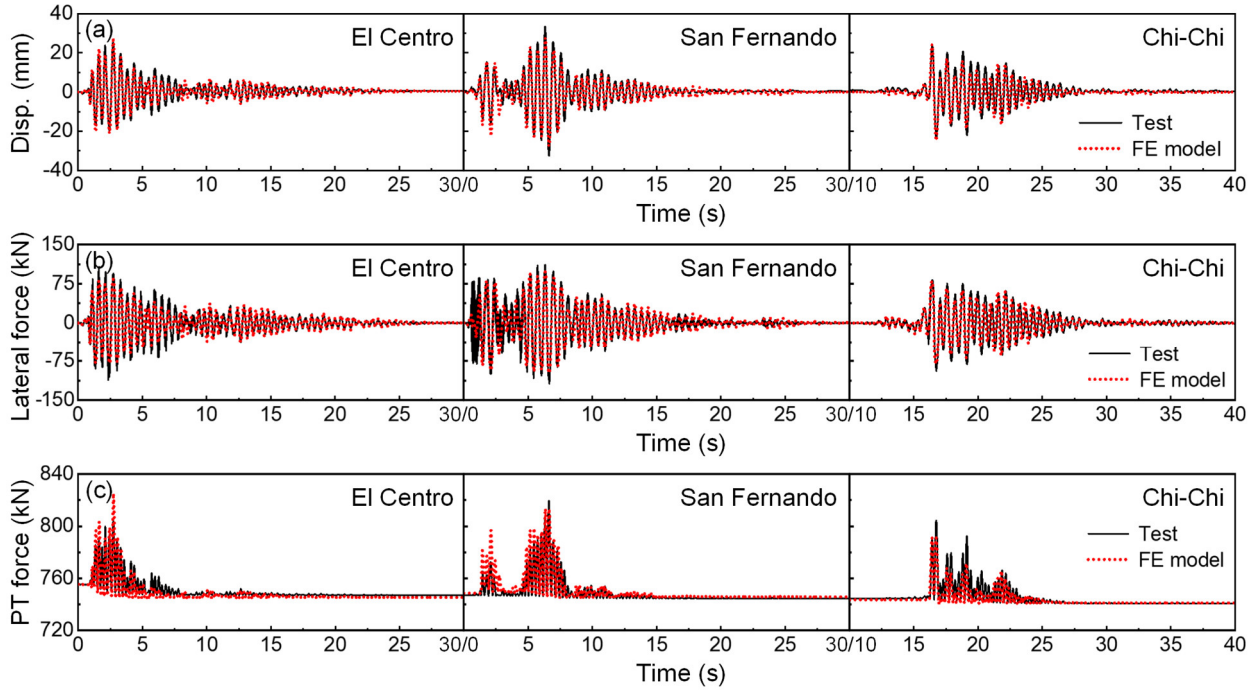

Figure 7. Comparisons between FE and test results of the two-rocking interface pier (i.e., the PRC+ST specimen) (a) displacement at the mass center; (b) lateral force of the pier; and (c) force in the PT bar.

4 Incremental Dynamic Analyses (IDAs) and results

The difference among the seismic responses of the three PRC piers was evaluated by performing IDAs. Two sets of ground motions were used, representing far-field and near-fault earthquake events, with velocity pulses observed in the near-fault cases. The median curves of the key seismic response parameters of three PRC piers are discussed in this section.

4.1 Earthquake recorders for the IDA

A total of 16 far-field and 16 near-fault ground motions selected from the Pacific Earthquake Engineering Research (PEER) Center database to match the code design spectrum were selected for the IDAs. The design

acceleration spectrum was defined according to the JTG/T B02-01-2008 specification (MOT, 2008) with a horizontal peak ground acceleration PGA = 1.0g, and a damping of 5%. The first set of earthquakes was an ensemble of 16 scaled far-field ground motion records (Moment magnitude, $M_w > 6.0$), as listed in Table 1. All far-field ground motions (*i.e.,* GM1 to GM16) were characterized by R_{rup} (*i.e.,* closest distance to rupture plane) greater than 17 km, and V_{s30} (*i.e.,* average shear velocity of top 30 m depth soil) ranging between 196.9 m/s and 452.9 m/s. The second set of earthquakes was an ensemble of 16 scaled near-fault ground motions, characterized by $R_{rup} < 8$ km and PGV/PGA ratio > 0.09 s. Table 2 summarizes the main characteristics of the near-fault records. Note that the near-fault earthquakes (*i.e.,* GM17 to GM32) were checked to ensure that the velocity pulse was observed within the corresponding velocity time history records, and the detailed period of the velocity pulse (T_p) is also given in the table.

Table 1. Characteristics of the 16 scalded far-field ground motions.

Name	Earthquake event, year	M_w	R_{rup} (km)	T_p (s)	V_{s30} (m/s)	PGV/PGA	SF
GM1	Kern County, 1952	7.4	38.9	***	385.4	0.098	3.00
GM2	Northern Calif-03, 1954	6.5	27.0	***	219.3	0.225	2.84
GM3	Borrego Mtn, 1968	6.6	45.7	***	213.4	0.205	4.55
GM4	San Fernando, 1971	6.6	22.8	***	316.5	0.098	2.04
GM5	San Fernando, 1971	6.6	29.0	***	452.9	0.125	3.75
GM6	San Fernando, 1971	6.6	39.5	***	298.8	0.102	5.29
GM7	Point Mugu, 1973	5.7	17.7	***	249.0	0.114	5.23
GM8	Tabas - Iran, 1978	7.4	28.8	***	324.6	0.129	4.52
GM9	Imperial Valley-06, 1979	6.5	24.6	***	205.8	0.123	4.46
GM10	Imperial Valley-06, 1979	6.5	22.0	***	242.1	0.114	1.74
GM11	Imperial Valley-06, 1979	6.5	21.7	***	237.3	0.116	3.46
GM12	Imperial Valley-06, 1979	6.5	17.9	***	196.9	0.151	3.12
GM13	Imperial Valley-06, 1979	6.5	22.0	***	249.9	0.139	3.79
GM14	Imperial Valley-06, 1979	6.5	36.9	***	212.0	0.113	4.38
GM15	Livermore-01, 1980	5.8	17.2	***	377.5	0.141	4.32
GM16	Victoria - Mexico, 1980	6.3	19.0	***	242.1	0.176	2.87

Table 2. Characteristics of the 16 scalded near-fault ground motions.

Name	Earthquake event, year	M_w	R_{rup} (km)	T_p (s)	V_{s30} (m/s)	PGV/PGA	SF
GM17	Tabas - Iran, 1978	7.4	2.1	6.19	766.8	0.118	0.60
GM18	Imperial Valley-06, 1979	6.5	4.0	4.13	205.6	0.094	1.11
GM19	Northridge-01, 1994	6.7	5.4	3.54	525.8	0.136	0.93
GM20	Northridge-01, 1994	6.7	5.9	1.37	269.1	0.131	0.88
GM21	Northridge-01, 1994	6.7	6.5	1.25	282.3	0.173	0.59
GM22	Northridge-01, 1994	6.7	5.4	2.98	251.2	0.190	0.76
GM23	Northridge-01, 1994	6.7	5.2	3.53	370.5	0.145	0.70
GM24	Northridge-01, 1994	6.7	5.3	2.44	440.5	0.131	0.97
GM25	Kobe - Japan, 1995	6.7	0.3	1.81	312.0	0.100	0.80
GM26	Chi-Chi - Taiwan, 1999	7.6	0.6	5.74	305.9	0.162	0.80
GM27	Chi-Chi - Taiwan, 1999	7.6	0.3	12.3	487.3	0.497	0.74
GM28	Darfield - New Zealand, 2010	7.0	1.2	6.23	344.0	0.155	0.72
GM29	Darfield - New Zealand, 2010	7.0	7.3	9.92	326.0	0.240	0.93
GM30	Darfield - New Zealand, 2010	7.0	7.1	7.37	263.2	0.240	1.11
GM31	Christchurch - New Zealand, 2011	6.2	2.0	4.83	206.0	0.139	0.99
GM32	Christchurch - New Zealand, 2011	6.2	5.1	1.55	141.0	0.132	1.12

Figure 8 shows the individual and mean acceleration spectra for the far-field and near-fault ground motion records together with the 5% damped design spectrum. Figure 8 shows that the mean acceleration spectrum of the 16 scaled far-field and near-fault records match well the design spectrum. The scale factors (SFs) of the record are listed in the tables and range between 0.59 and 5.29.

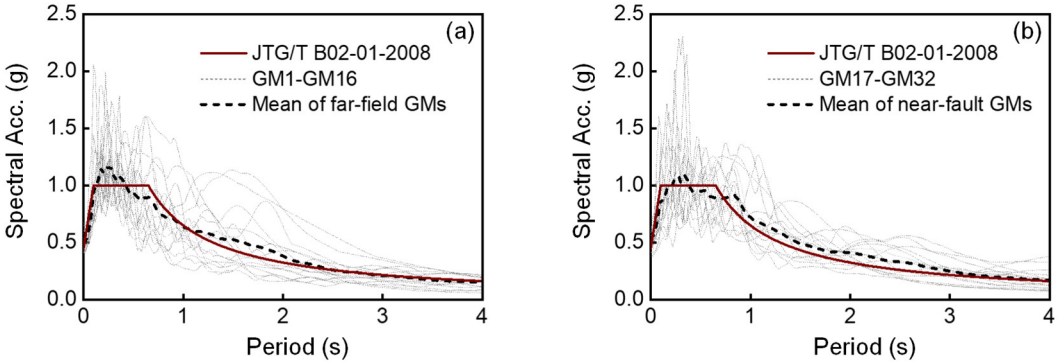

Figure 8. Acceleration response spectra: (a) 16 scaled far-field ground motions; (b) 16 scaled near-fault pulse-like ground motions.

4.2 Results and discussion

Figure 9 provides the displacement and velocity responses at the center of mass of three PRC rocking interface systems under the two sets of ground motions. As shown in Figure 9(a), a slight difference was observed between the IDA displacement curves of three PRC piers. In general, the results show that increasing the number of interfaces corresponds to an increase in the displacement response for the PRC pier. This was expected because of the longer fundamental period of PRC piers with more rocking interfaces (*i.e.,* 0.38, 0.44, and 0.48 s for the case with one, two, and three interfaces), resulting in a relatively larger displacement demand. In addition, the near-fault records procured larger displacements compared to the far-field records, especially for relatively high ground motion intensities (*i.e.,* PGA > 0.3 g). For example, the far-field ground motions with a PGA = 0.60g induced a maximum displacement of approximately 5 cm, comparable to the displacement values obtained by near-fault records with PGA = 0.45g. A similar phenomenon was also observed in the test results of Shen *et al.* (2023b). As expected, the near-fault (pulse-like) records also produced larger velocity responses of the PRC piers. Figure 9(b) shows that for PGA > 0.60g, the velocity demand at the mass center under near-fault ground motions was significantly larger than that induced by the far-field ground motions. For a PGA = 1.2g, the velocity reached approximately 0.80 and 0.95 m/s for the far-field and near-fault ground motions, respectively, the former being only ~85% of the latter. Moreover, it is noteworthy that the IDA velocity curves of the PRC piers with one, two, and three rocking interfaces were almost identical, implying that the influence of interface number on the velocity response for PRC piers was minimal. This is because the velocity spectrum values remained relatively constant for the range of fundamental periods of the three PRC piers (*i.e.,* 0.38s to 0.48s).

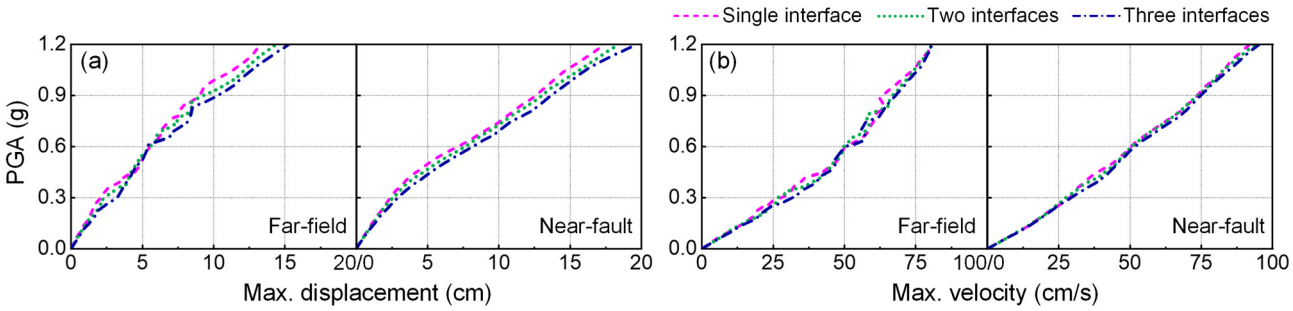

Figure 9. IDA curves of the responses at the mass center: (a) maximum displacement; (b) maximum velocity.

In light of the previous discussion [*i.e.,* Figure 7(c)], the force in the PT bar was of great concern because both the increase and loss phenomena occurred, affecting the pier's self-centering capacity. Figure 10 compares the maximum and loss of the PT force among the different rocking interfaces at various PGA levels. Note that the PT bar always remained elastic throughout the IDA analyses as the simulation maximum PT forces were still less than the nominal yield strength of the PT bar (*i.e.,* 1341 kN, Shen *et al.* 2023b). It was also observed that the single interface PRC pier exhibited the greatest PT force demand under both far-field and near-fault ground motions [Figure 10(a)]. This is related to the highly non-linear behavior of the case with multiple rocking interfaces and is strongly affected by higher mode effects (Marzok and Lavan 2021). Conversely, the case

with three rocking interfaces had the maximum loss of PT force, as shown in Figure 10(b). This is expected because the larger displacement excursion [Figure 9(a)] would induce a more pronounced loss of PT force. In addition, by comparing the PT force responses between the far-field and near-fault ground motions, it was found that the effect of the velocity pulse on the response of PT bar was significant, and the pulse-like excitations easily triggered a larger PT force increase when the gap was opened resulting in a large PT loss after the rocking motion was completed.

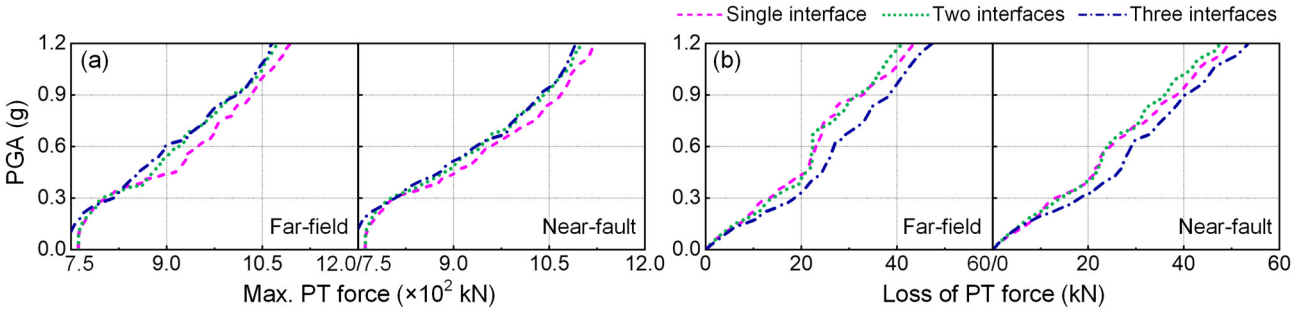

Figure 10. IDA curves of the PT bar responses: (a) maximum PT force; (b) loss of PT force.

The variation of PT force had the potential disadvantages to the self-centering capacity of the PRC pier. Figure 11 illustrates the IDA curves of self-centering responses in terms of the residual displacement (δ_{res}) [Figure 11(a)] and the relative self-centering efficiency (RSE) [Figure 11(b)]. The RSE represents the ratio between the recoverable displacement and the peak displacement, δ_{peak} (Shen *et al.* 2022), and can be calculated as:

$$RSE = 1 - \frac{\delta_{res}}{\delta_{peak}} \quad (1)$$

The RSE = 1.0 represents the perfect self-centering behavior. Figure 11 shows that the residual displacement of three PRC piers was almost neglectable for PGA < 0.5g. Beyond this seismic intensity level, some residual displacement was observed. In addition, the results show that the PRC pier with a single rocking interface provides a relatively better self-centering capacity, mainly due to the lower peak displacement demand [Figure 9 (a)], but it generates a relatively more significant PT force [Figure 10 (a)]. However, it should be noted that all three PRC piers showed a 'good' self-centering behavior during the IDAs, with RSE values ranging between 0.85 and 1.0. As to the effect of the velocity pulse, it can be observed that the velocity pulse, to some extent, slightly contributed to the enhancement of PRC piers' self-centering capacity.

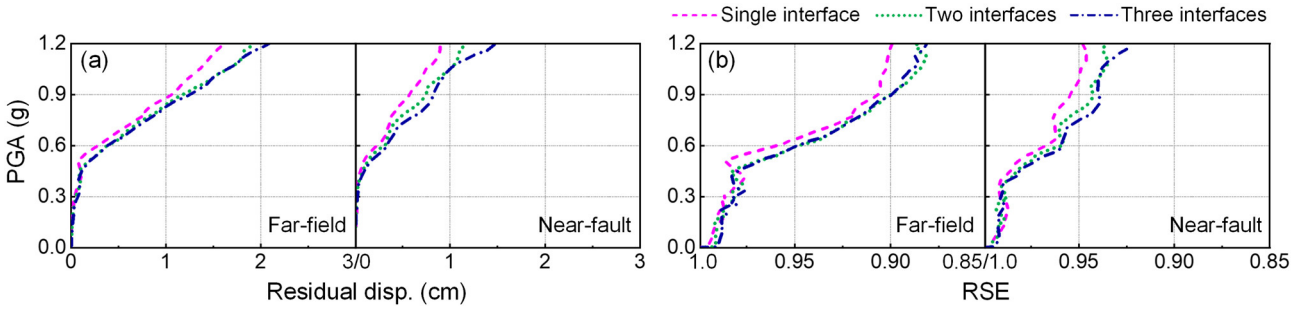

Figure 11. IDA curves of the self-centering responses: (a) residual displacement; (b) RSE.

Figure 12 shows the comparison and the evolution of the shear forces for the three PRC piers. All piers showed shear forces increasing with the PGA until a force of approximately 90 kN corresponding to a PGA = 0.6g. After that, the larger PGA would not significantly increase the pier's shear force response due to the obvious rocking isolation. In addition, the IDA curves of shear force among three PRC piers and two sets of ground motions were generally close, indicating that the effects of the number of rocking interfaces and the velocity pulse on the lateral force were limited in PRC piers.

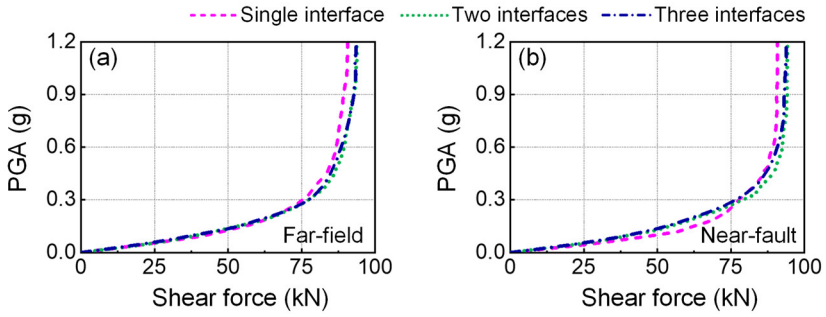

Figure 12. IDA curves of the shear force under: (a) far-field ground motions; (b) near-fault ground motions.

5 Conclusions

The present paper investigates the effects of the number of rocking interfaces and the velocity pulse of the ground motions on the seismic performance of unbonded post-tensioned reinforced concrete (PRC) piers. Numerical simulations were performed using detailed 3D Finite Element (FE) models validated against experimental results. Three rocking interface scenarios, *i.e.,* the piers with a single rocking interface at the base, with two and three rocking interfaces along the column height, were considered, and their seismic response was assessed and compared through Incremental Dynamic Analyses (IDAs) using suites of far-field and near-fault earthquakes. The PT force loss was also modeled for realistic rocking response scenarios.

The results show that the PRC pier with three rocking interfaces experienced larger peak displacements regardless of seismicity level. Consequently, it was characterized by more significant PT force loss and larger residual deformations with respect to the other two piers. The single rocking PRC pier showed a relatively superior self-centering capacity thanks to its larger PT force increase and lower PT force loss. However, the larger PT force in the single rocking case did not contribute to an enhancement in its lateral force, and all three piers had almost a similar shear force demand at all seismic intensity levels. In addition, there was also a negligible difference in velocity responses among the three PRC piers. Also, the results show that the pulse-like feature of the earthquakes can amplify the piers' lateral displacement, the PT force, and the self-centering capacity, all related to the deformation of the pier, and this phenomenon was more obvious at higher intensities. In contrast, its effect on the shear force of the PRC piers was limited due to the rocking isolation.

6 References

Billington S.L., Yoon J.K. (2004). Cyclic response of unbonded posttensioned precast columns with ductile fiber-reinforced concrete, *ASCE Journal of Bridge Engineering*, 9(4): 353-363.

Bu Z.Y., Ou Y.C., Song J.W., Zhang N.S., Lee G.C. (2016). Cyclic loading test of unbonded and bonded posttensioned precast segmental bridge columns with circular section, *ASCE Journal of Bridge Engineering*, 21(2): 04015043.

Elettore E., Freddi F., Latour M., Rizzano G. (2022). Parametric study and finite element analysis of self-centring steel column bases with different structural properties, *Journal of Constructional Steel Research*, 199: 107628.

Elettore E., Lettieri M., Freddi F., Latour M., Rizzano G. (2021). Performance-based assessment of seismic-resilient steel moment resisting frames equipped with innovative column base connections, *Structures*, 32: 1646-1664.

Freddi F., Dimopoulos C.A., Karavasilis T.L. (2020). Experimental evaluation of a rocking damage-free steel column base with friction devices, *ASCE Journal of Structural Engineering*, 146(10): 04020217.

Freddi F., Galasso C., Cremen G. Dall'Asta A., Sarno L.D., Giaralis et al. (2021). Innovations in earthquake risk reduction for resilience: Recent advances and challenges, *International Journal of Disaster Risk Reduction*, 60: 102267.

Guerrini G., Restrepo J.I., Vervelidis A., Massari M. (2015). *Self-centering precast concrete dual-steel-shell columns for accelerated bridge construction: Seismic performance, analysis, and design*, PEER Report 2015/13, University of California, Berkeley: Pacific Earthquake Engineering Research Center.

Hassanli R., Youssf O., Mills J.E. (2017). Seismic performance of precast posttensioned segmental FRP-confined and unconfined crumb rubber concrete columns, *ASCE Journal of Composites for Construction*, 21(4): 04017006.

Kwan W.P., Billington S.L. (2003a). Unbonded posttensioned concrete bridge piers. I: Monotonic and cyclic analyses, *ASCE Journal of Bridge Engineering*, 8(2): 92-101.

Kwan W.P., Billington S.L. (2003b). Unbonded posttensioned concrete bridge piers. II: Seismic analyses, *ASCE Journal of Bridge Engineering*, 8(2): 102-111.

Li Y.X., Li J.Z., Shen Y. (2021). Quasi-static and nonlinear time-history analyses of post-tensioned bridge rocking piers with internal ED bars, *Structures*, 32: 1455-1468.

Lu X.L., Fu G.K., Shi W.X., Lu W.S. (2008). Shake table model testing and its application, *The Structural Design of Tall and Special Buildings*, 17(1): 181-201.

Marriott D., Pampanin S., Palermo A. (2009). Quasi-static and pseudo-dynamic testing of unbonded post-tensioned rocking bridge piers with external replaceable dissipaters, *Earthquake Engineering and Structural Dynamics*, 38(3): 331-354.

Marzok A., Lavan O. (2021). Seismic design of multiple-rocking systems: A gradient-based optimization approach, *Earthquake Engineering and Structural Dynamics*, 50(13): 3460-3482.

Mashal M., Palermo A. (2019). Low-damage seismic design for accelerated bridge construction, *ASCE Journal of Bridge Engineering*, 24(7): 04019066.

Mazzoni S., McKenna F., Scott M. H., Fenves G. L. (2009). *OpenSees: Open system for earthquake engineering simulation*, University of California, Berkeley: Pacific Earthquake Engineering Research Center.

MOT (2008). *JTG/T B02-01-2008. Guideline for seismic design of highway bridges*, Ministry of Transport of the People's Republic of China, Beijing.

NCHRP (2011). *REPORT 698. Application of accelerated bridge construction connections in moderate-to-high seismic regions*, National Cooperative Highway Research Program, Washington, DC.

Shen Y., Freddi F., Li Y.X., Li J.Z. (2022). Parametric experimental investigation of unbonded post-tensioned reinforced concrete bridge piers under cyclic loading, *Earthquake Engineering and Structural Dynamics*, 51(15): 3479-3504.

Shen Y., Freddi F., Li Y.X., Li J.Z. (2023a). Enhanced strategies for seismic resilient posttensioned reinforced concrete bridge piers: Experimental tests and numerical simulations, *ASCE Journal of Structural Engineering*, 149(3): 04022259.

Shen Y., Freddi F., Li Y.X., Li J.Z. (2023b). Shaking table tests of seismic-resilient post-tensioned reinforced concrete bridge piers with enhanced bases, *Engineering Structures*, accepted.

Trono W., Jen G., Panagiotou M., Schoettler M., Ostertag C.P. (2015). Seismic response of a damage-resistant recentering posttensioned-HYFRC bridge column, *ASCE Journal of Bridge Engineering*, 20(7): 04014096.

Yamashita R., Sanders D.H. (2009). Seismic performance of precast unbonded prestressed concrete columns, *ACI Structural Journal*, 106(6): 821-830.

Zhong X.Q., Li Y.X., Li J.Z., Shen Y., Bao Z.H. (2022). Seismic performance of self-centering bridge piers with rocking mechanical hinges, *ASCE Journal of Bridge Engineering*, 27(12): 04022122.